EDGE ARTICLE

Check for updates

All publication charges for this article have been paid for by the Royal Society of Chemistry

A general graph neural network based implicit solvation model for organic molecules in water†

Paul Katzberger [ID] and Sereina Riniker [ID] *

The dynamical behavior of small molecules in their environment can be studied with classical molecular dynamics (MD) simulations to gain deeper insight on an atomic level and thus complement and rationalize the interpretation of experimental findings. Such approaches are of great value in various areas of research, *e.g.*, in the development of new therapeutics. The accurate description of solvation effects in such simulations is thereby key and has in consequence been an active field of research since the introduction of MD. So far, the most accurate approaches involve computationally expensive explicit solvent simulations, while widely applied models using an implicit solvent description suffer from reduced accuracy. Recently, machine learning (ML) approaches that provide a probabilistic representation of solvation effects have been proposed as potential alternatives. However, the associated computational costs and minimal or lack of transferability render them unusable in practice. Here, we report the first example of a transferable ML-based implicit solvent model trained on a diverse set of 3 000 000 molecular structures that can be applied to organic small molecules for simulations in water. Extensive testing against reference calculations demonstrated that the model delivers on par accuracy with explicit solvent simulations while providing an up to 18-fold increase in sampling rate.

1 Introduction

Classical molecular dynamics (MD) is a widely used approach that employs Newton's equation of motion to provide insights into the dynamical processes of molecules, ultimately allowing rationalization of experimental findings and supporting drug discovery in general (for examples see ref. 1–3). Much progress has been made in efficiently exploring the conformational space of molecules in a given environment. The development of specialized hardware,[4] highly parallelized algorithms,[5] and enhanced sampling methods[6] continues to push the frontier of accessible timescales. A key aspect of exploring the correct conformational space of a molecule is solvation effects. To capture the local solvation effects correctly, the solvent molecules around a molecule (typically in their thousands) are typically modelled explicitly in the simulation. However, this explicit treatment of solvation results in a large number of degrees of freedom in the system, which is computationally expensive (computational cost per simulation step scales between $O(N)$ and $O(N^2)$ where N is the number of atoms). The larger number of degrees of freedom leads additionally to a more rugged free-energy surface, which decreases the effective sampling rate further.[7] Hence, the majority of the

computational cost is spent on solvent–solvent interactions, which are typically not of interest *per se*.

The alternatives to this approach are implicit solvent methods, which model the mean effect of a given environment on the solute in a probabilistic fashion.[7] Most of these implicit solvents rely on continuum approaches where the effect of an equidispersed medium on a given molecule is calculated. While many of them are indeed much faster than their explicit counterpart, the major drawback of these methods is that they do not describe the local solvation effects correctly. Based on recent successes of applying machine learning (ML) in the field of chemistry,[8] ML-based approaches have been developed to learn the effects of a given environment (solvent) on a solute.[9–13] These models are either too slow and/or not sufficiently transferable between different molecules to be practically usable in MD simulations, leaving explicit solvent simulations as the only reliable solution for generating accurate conformational ensembles in solution.

In this work, we showcase a novel ML-based implicit solvent model using a graph neural network (GNN) that is applicable to diverse small organic molecules, achieving the accuracy of explicit-solvent simulations but in a fraction of the time. To the best of our knowledge this is the first instance of a truly transferable ML-based implicit solvent method covering a vast organic chemical space while achieving high accuracy. The approach is validated against explicit solvent reference simulations by comparing predicted mean forces of an external test set as well as by performing prospective MD simulations. To

Department of Chemistry and Applied Biosciences, ETH Zürich, Vladimir-Prelog-Weg 2, 8093, Zürich, Switzerland. E-mail: sriniker@ethz.ch

† Electronic supplementary information (ESI) available. See DOI: https://doi.org/10.1039/d4sc02432j

highlight the substantial improvements over state-of-the-art implicit solvents, the commonly used GB-Neck2 implicit solvent[14] is taken as a point of reference.

1.1 Background

Standard implicit solvent models largely rely on estimating the mean energies and forces of a given environment exerted on a solute by modeling the solvent as a continuum. For instance, the polar contribution of the solvation free energy can be calculated by the effect of a dielectric continuum on the solute. Examples of such approaches would be Poisson–Boltzmann (PB),[15] fast analytical continuum treatments of solvation (FACTS),[16] or generalised Born (GB) methods.[17] Similarly, the non-polar contribution is typically modeled as a linear function of a molecule's surface area.[18] These simplifications are likely responsible for the inability of these kinds of models to accurately describe local solvation effects. This is most pronounced in cases where the discrete nature of the solvent molecules yields a density distribution that diverges from a continuum description at the solute–solvent interface. Examples for this behavior can be found in previous studies,[12,19] as well as in the Results section of this work.

ML approaches have also been applied to model the effects of a given solvent environment on molecules.[9–13] While these models are indeed capable of reproducing desired effects (*e.g.*, reproduction of conformational ensembles or free-energy profiles) and dramatically outperform the standard implicit solvent methods in reproducing explicit solvent reference calculations, they currently have two major limitations for practical usability. First, even though much smaller systems were studied (*i.e.*, only the molecule of interest and not a solvated box) these ML based approaches were considerably slower than the explicit solvent reference. As the rather young field of ML potentials (*i.e.*, the broader field of applying ML models to describe the Hamiltonian in MD simulations) develops further, we expect this issue to be reduced as many of the optimisations for classical MD developed over the last half century still need to be introduced for these applications (*e.g.*, parallel evaluation of all parts of the Hamiltonian or usage of pairlist algorithms).[20] The second issue and hence the truly limiting one is, however, that the ML models are currently either not or only partially transferable from one molecular system to the next. In practice, this means that the current ML approaches need to be re-trained every time a new system or class of systems is studied (including generation of suitable training data), rendering them impractical for most common applications.

Recently, we developed a GNN that utilized a Δ-ML scheme for modeling solvation effects, which showed promising transferability within a relatively narrow set of similar small peptides.[12] In this methodology, a three layer GNN was inserted into the functional form of the classical GB-Neck2 implicit solvent[14] model. The rationale behind this approach is that while the forces exerted on a solute estimated by a continuum are not accurate, they provide the GNN with a good starting point. Specifically, the long-range effects are already well represented by the classical implicit solvent, and the GNN needs to learn only a correction for the short-range (local) effects.

In the work presented here, the functional form of the GNN model was further refined by introducing an additional separate term accounting for the non-polar interactions that does not rely on the generalized Born radii as commonly used in GBSA models or in our previous model,[12]

$$\Delta G_{\text{non-polar}} = \sum_i^N S\big(\phi\big(R, q, r_{\text{a}}, r, R_{\text{cutoff}}\big)\big) \cdot \gamma \cdot (r_i + r_{\text{w}})^2, \quad (1)$$

where S is the sigmoid function, ϕ the GNN, R the GB-Neck2 Born radii, q the partial charges, r_{a} the atomic radii of all atoms, r the distances between all atoms, R_{cutoff} the cutoff radius, γ the slope, r_i the atomic radius of atom i, and r_{w} the probe sphere radius of water. This functional form builds upon findings by Schäfer and Karplus,[18] who demonstrated a good correlation between the solvent accessible surface area (SASA) and the solvation free energy. An illustration of the model architecture is provided in Fig. S1 in the ESI.†

It should be noted that even though this functional form has experimental as well as theoretical foundations, the incorporation of the GNN renders it a numerical potential. While the prediction of the GNN represents the fraction of an atom that is accessible by the solvent, its numerical values do not necessarily correspond to the analytical solution. Both scalings in the polar and non-polar parts of the GNN architecture are related to the level of screening exerted from intramolecular atoms. To allow for synergistic effects as well as to introduce a certain level of flexibility, a multitask approach was chosen where the GNN predicts two instead of one value per atom (*i.e.*, for each atom a scaling factor for the polar and the non-polar part of the solvation free energy is predicted). During training, both terms are fit together, further diluting the direct correlation between the classical functional form and the resulting potential. The GNN model is trained on a diverse data set consisting of 369 486 small molecules (molecular weight <500 Da) designed to cover a large fraction of the organic chemical space.[21] For each molecule, the mean forces exerted by the solvent environment are calculated for up to nine conformations leading to 3 208 720 data points in total. The employed approach shares similarities with the average solvent environment configuration (ASEC)[22,23] approach, which was recently applied by Yao *et al.*[24] for the training of an ML potential.

A substantial benefit of explicit solvent simulations is that they work for any solvent (given corresponding force-field parameters). Currently, ML-based solvent models need to be trained on a specific solvent in order to accurately describe it. In this study, the focus lies on developing a replacement for explicit water simulations. The aqueous environment is not only one of the most studied but also one of the most computationally expensive solvents, as water has a high atomic density. In addition, its ability to form multiple hydrogen bonds makes it especially challenging for implicit solvents to describe the local solvation effects.

2 Results and discussion

2.1 Timings and external test set

As computational efficiency is crucial for practical usability (*i.e.*, the implicit solvent model must be faster than explicit-solvent simulations, which is not achieved by many of the proposed ML models[11–13]), we first investigated the effect of the complexity of the GNN architecture on simulation speed. For this, we varied the number of parameters in the GNN (*i.e.*, the size of the hidden layers in the multi-layer perceptrons (MLPs)) from 128 to 96, 64, and 48 when training on our set of 369 486 diverse small molecules with molecular weight <500 Da. The prediction accuracy of the four GNN architectures was compared on an external test set containing 1000 compounds with molecular weight ranging from 500 Da to 700 Da (see Table S1 in the ESI† for a compilation of the test-set performance assessed by the most common metrics). Current neural network implementations are focused on optimising parallel operations rather than consecutive ones. For MD applications, this is problematic as the foundations of MD rely on fast consecutive evaluations of the Hamiltonian. To utilise the full potential of current graphics processing unit (GPU) models as well as to follow good MD practices,[25] we simulated multiple replicates of a molecule at once and compared the cumulative simulation times with explicit solvent TIP3P simulations (Fig. 1A). A summary of absolute timings for the different solvent models is shown in the ESI (Table S2†). An almost linear relationship between the simulation speed and the test set RMSE can be observed, which is to be expected as the larger number of parameters allows the model to increase accuracy at the cost of more computations when evaluated. Importantly, all four GNN architectures provide a significant speed-up over the explicit-solvent simulations (*i.e.*, by factors of 2.5, 3.2, 4.4, and 5.4, respectively). While the test set RMSE increases with decreasing hidden layer size, it is noteworthy that the relative error increment between the architectures remains low (*e.g.*, the relative difference in test set

RMSE for the model with a hidden size of 128 *versus* 64 is only 13%). A key aspect of implicit solvent models is that they can provide comparable insights at lower computational cost. Following this argument, we decided to use in the following the GNN with a hidden layer size of 64 as it reduces computational cost by 4.4-fold while still achieving high accuracy on the external test set (Fig. 1B).

2.2 Prospective molecular dynamics simulations

The low RMSE on the external test set indicates that the model is transferable between different sets of compounds. However, recently it was discovered that accurate force predictions on a test set do not necessarily correlate with accurate and stable simulations.[26] Hence, the GNN is further evaluated by performing prospective MD simulations of compounds not included in the training set. While we trained three models per architecture with different initialisation to assess the variance in the previous section, a single GNN is used to carry out the simulations, mimicking how the approach would be used in practice. To be conservative, we chose the model with the highest external test set RMSE for this. Note that we have repeated the computational experiments with the other two models and the results are qualitatively equivalent (see Fig. S14–S21 in the ESI†).

2.2.1 Intramolecular hydrogen bonds in water. A frequently cited limitation of current implicit solvent models for water is that they do not accurately capture the balance between conformations with and without intramolecular hydrogen bonds, *i.e.*, conformations with intramolecular hydrogen bonds are typically overstabilized. To assess whether the GNN accurately describes this balance, we used a test set of 15 small molecules (set **I**, see Fig. 2A) from the FreeSolv database[27] that can form intramolecular hydrogen bonds. Note that none of these molecules have been included in the training or validation sets. For each molecule, the free-energy profile of the intramolecular hydrogen bond was calculated with the GNN,
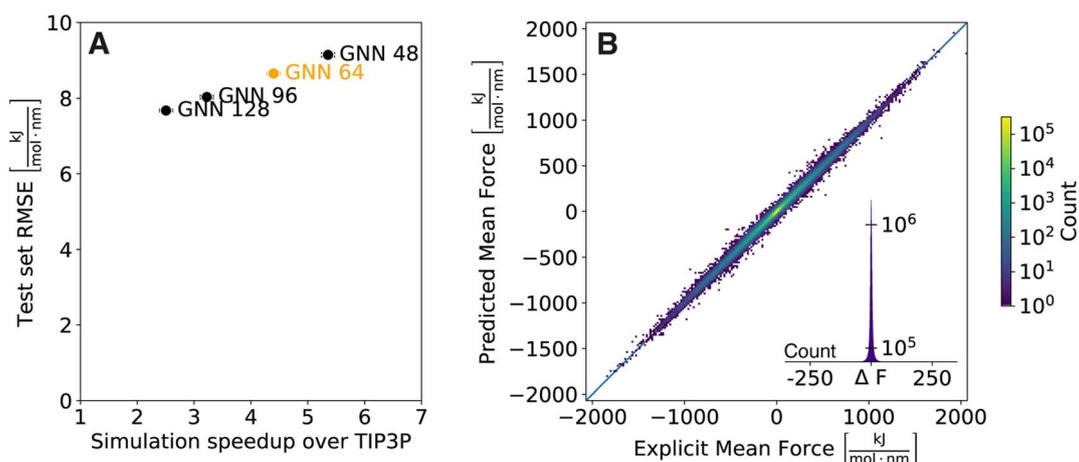

Fig. 1 (A) Comparison of GNN architectures with varying size of hidden layers (128, 96, 64, and 48). The increase in cumulative simulation speed of 256 replicates over an explicit solvent TIP3P simulation is plotted against the test set RMSE. The standard deviation over the GNN replicates is denoted by error bars. (B) Comparison of predicted and reference forces for the test set. Results are shown for one replicate of the GNN with a hidden layer size of 64.
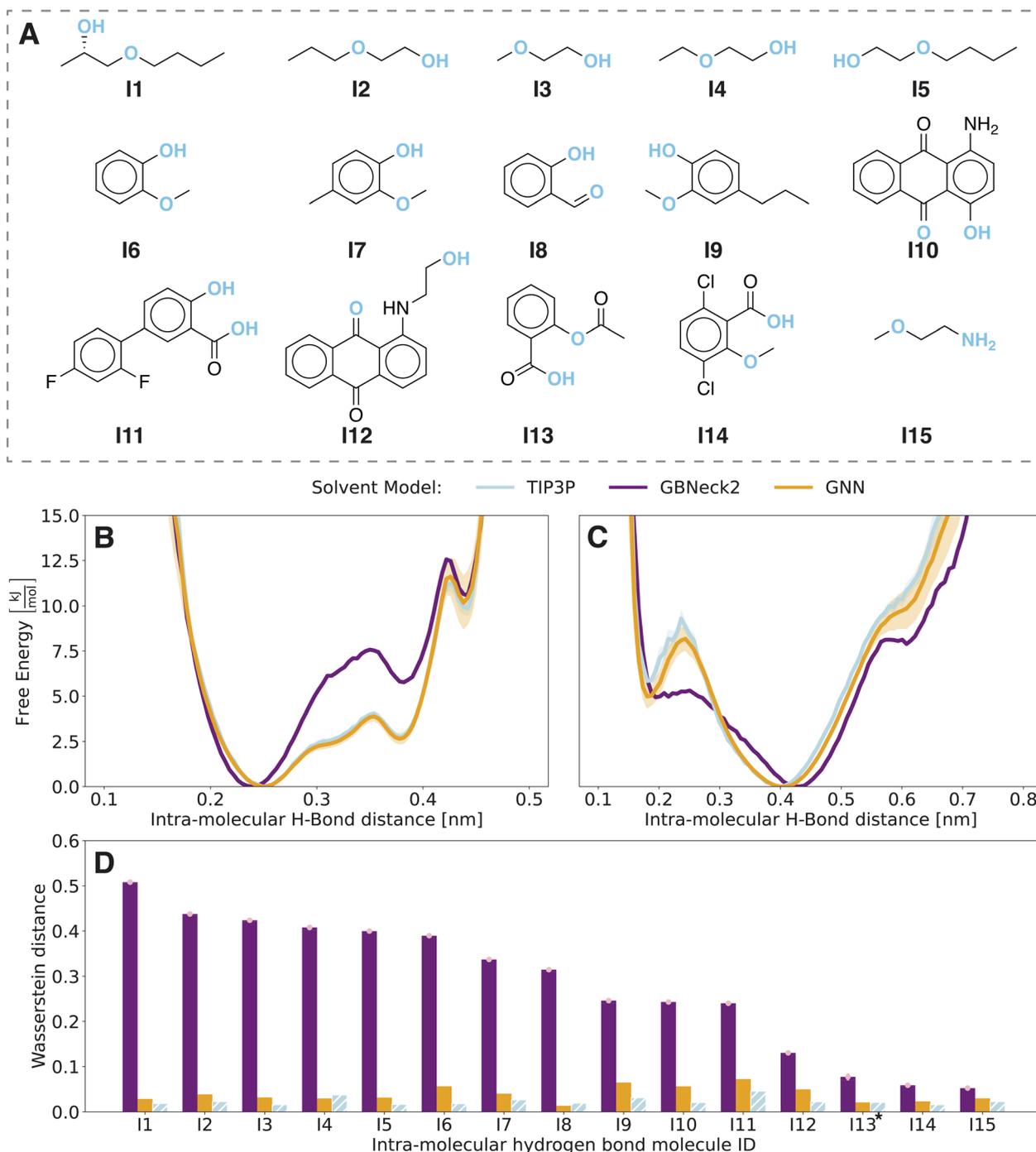
Fig. 2 Comparison of the GNN implicit solvent model (orange, 128 × 5 ns) with the explicit solvent TIP3P model (blue, 1 × 500 ns) and the baseline implicit solvent GB-Neck2 model (purple, 3 × 500 ns). (A) Compound set **I** ordered by GB-Neck2 Wasserstein distances in panel D. The studied hydrogen-bond donor and acceptor pair is indicated in blue. (B) Free-energy profile of the opening of the intramolecular hydrogen bond of compound **I1**. (C) Free-energy profile of the opening of the intramolecular hydrogen bond of compound **I12**. (D) Wasserstein distances of implicit solvent models compared to the explicit solvent TIP3P reference. For comparison, the hatched blue bar indicates the Wasserstein distance of the first half of the TIP3P simulation *versus* the second half. Pink error bars represent the standard deviation over multiple replicates of the GB-Neck2 model.

the baseline GB-Neck2 implicit solvent model, and from explicit solvent TIP3P reference simulations. Fig. 2B and C show the profiles for compounds **I1** and **I12** as examples (see Fig. S2 in the ESI† for the other compounds). In general, the GNN approach matches the TIP3P reference calculations very well while the GB-Neck2 model often misrepresents the hydrogen-bond interactions and shows large deviations in the free-energy profiles. In case of compound **I1** (Fig. 2B), the

intramolecular hydrogen bond is overstabilized, leading to a shift of the global minimum to shorter distances as well as to higher free-energy values for the first local minima at approximately 0.38 nm. This behavior seems to be characteristic for hydrogen bonds leading to pseudo five-membered rings. For compound **I12** (Fig. 2C), the global minimum is also shifted, however, to larger distances. A striking difference can also be observed for a local minimum at 0.18 nm. While the minimum is clearly visible for the TIP3P and GNN simulations, the GB-Neck2 model does only show a saddle point. One reason for this behavior could lie in the continuum nature of the GB-Neck2 model. As no notion of the binary nature of explicit solvation effects is considered, the model fails to accurately describe two distinct conformational states, *i.e.*, the direct hydrogen bond (at 0.18 nm) and the indirect hydrogen bond mediated by a water molecule (at 0.4 nm).

For a quantitative assessment, the underlying probability distributions of the free-energy profiles of the implicit solvent models (Fig. S3 in the ESI†) were compared to the TIP3P reference using the Wasserstein distance[28] (Fig. 2D). The Wasserstein distance has its origins in optimal transport and calculates the cost of transforming one probability distribution into another, *i.e.*, the lower the distance the more similar the two distributions are. To exclude differences due to finite sampling, we checked the convergence of the Wasserstein distance (see Fig. S3 in the ESI†). Compounds **I8** and **I13** showed non-converged results and hence both simulations were elongated by 10-fold. Even with the extended simulation time, these issues persisted for compound **I13** with respect to a second intramolecular hydrogen bond of the carboxy group. For a fair comparison, the free-energy profiles and corresponding probability distributions were only analyzed for the more populated state of intramolecular hydrogen bonds within the carboxy group of distance <0.27 nm. To assess the variance within explicit-solvent simulations, the reference TIP3P simulation was divided into two parts and the Wasserstein distance between the first half and the second half of the simulation was calculated (blue bars in Fig. 2D). For all molecules in set **I**, the
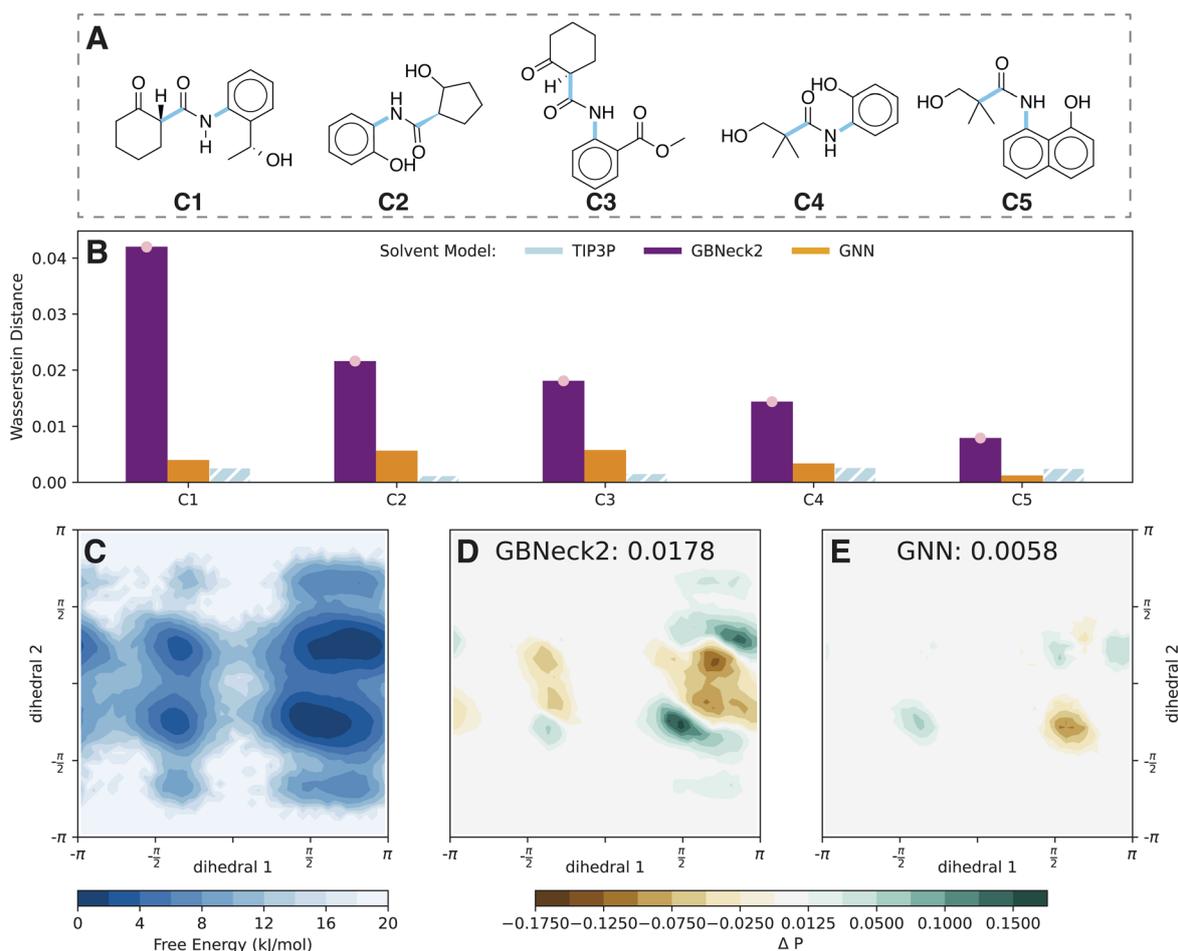

Fig. 3 Comparison of the GNN implicit solvent model (orange, 128 × 10 ns) with the explicit solvent TIP3P reference (blue, 1 × 500 ns) and the baseline implicit solvent GB–Neck2 model (purple, 3 × 500 ns). (A) Compound set **C** ordered by GB–Neck2 Wasserstein distances in panel B. The studied torsional angles are indicated in blue. (B) Wasserstein distances of implicit solvent models compared to the TIP3P reference. For comparison, the hatched blue bar indicates the Wasserstein distance of the first half of the TIP3P simulation *versus* the second half. (C) Probability distribution along the two central torsion angles (marked blue in panel A) of compound **C3** produced using the TIP3P solvation model. (D) Difference in probability distribution for the GB–Neck2 and TIP3P simulations for compound **C3**. (E) Difference in probability distribution for the GNN and TIP3P simulations for compound **C3**.

GNN approach outperforms the GB-Neck2 model with significantly smaller Wasserstein distances.

2.2.2 Conformational ensemble. To further analyze the performance of the GNN approach, we performed MD simulations of a set of five compounds (set **C**, see Fig. 3A) whose conformational ensemble can be well described by two major rotatable bonds. Again, the Wasserstein distance metric can be used to compare the 2D probability distributions. For all five molecules, the Wasserstein distance with respect to the TIP3P reference was much smaller for the GNN than for the GB-Neck2 model (Fig. 3B), indicating that ensembles could be accurately described.

A good example for the observed differences is compound **C3**, for which the 2D probability distribution along the two central torsional angles is shown in Fig. 3C. The difference plots in probability distributions are shown in Fig. 3D and E for the GB-Neck2 and GNN models, respectively. While there are only minor differences for the GNN, the GB-Neck2 model systematically shifts the distribution of dihedral 2 closer to 0 rad. In addition, the asymmetric nature of the two global minima is only captured by the GNN model.

2.3 Effective sampling rates

The analyses above indicate that the GNN model is capable of generating results on par with TIP3P explicit solvation, making it a valuable tool to study solvation effects in water at lower computational costs. In addition to a (dramatic) reduction of the number of degrees of freedom in the system with implicit solvation, the effective sampling rate of such a simulation should be higher due to a smoothing of the free-energy surface. In order to study and quantify this effect, the speed at which the conformational space is explored was compared for the GNN and TIP3P simulations of set **C**. For this, the conformations were clustered for each compound using the energy based clustering (EBC) algorithm,[29] and the number of unique clusters found after a given number of simulation frames (write-out frequency every 100 simulation steps) served as a metric for sampling speed. The clustered free-energy surfaces as well as the cluster assignments are shown in Fig. S5–S9 in the ESI.† For all five compounds, the GNN simulations visit more clusters within the same number of frames as the TIP3P explicit solvent model. This is shown for compound **C3** in Fig. 4A and for compounds **C1**, **C2**, **C4**, and **C5** in Fig. S10–S13 in the ESI.† The difference in the effective sampling rate of the GNN relative to the TIP3P model can be quantified by artificially increasing the speed of the TIP3P simulations (*i.e.*, an effective speed-up by factors of 2, 3, 4, and 5 was achieved by constructing new trajectories considering every second, third, fourth, and fifth frame of the TIP3P simulation, respectively). Fig. 4B summarizes these results for the five compounds, showing the average number of visited clusters after 1000 frames (indicated by the vertical dashed line in Fig. 4A). The achieved effective sampling speed-up for the GNN implicit solvent model over the reference TIP3P simulations ranges from a factor of 3 to 5 depending on the studied system. Interestingly, the increase in effective sampling rate is highest for compounds **C2** and **C4**, which feature the largest barriers to cross. This observation is in line with the findings by Anandakrishnan *et al.*,[30] who observed that implicit solvent simulations exhibit a higher increase in effective sampling rate compared to explicit solvent simulations as the magnitude of the conformational flexibility increases. This may present a further benefit of the GNN approach as overcoming the highest energy transitions faster is especially desirable. In this context, it is noteworthy that this increase in effective sampling rate by approximately a factor of 4 is on top of the lower computational cost of the GNN (by a factor of 4.4). As the two factors are multiplicative, an overall increase in sampling speed of approximately 18-fold is achieved.
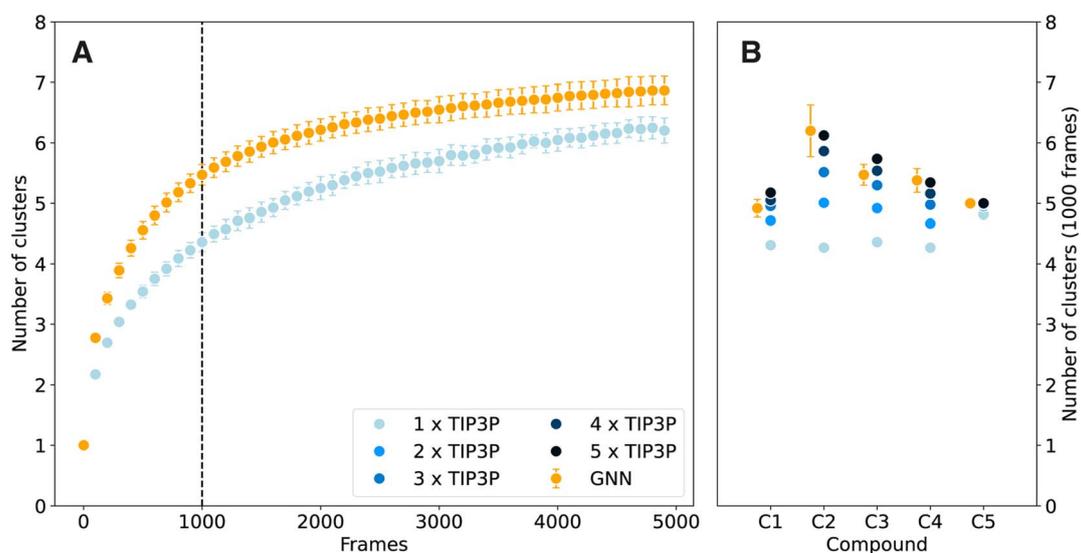

Fig. 4 Comparison of the effective sampling rate between the GNN implicit solvent model (orange) and the explicit TIP3P reference (blue). (A) Comparison of the average number of visited clusters after a given number of MD steps for compound **C3**. (B) Comparison of the average number of visited clusters after 1000 frames for all compounds.

3 Conclusions

In this study, we presented a novel ML approach to learn the mean solvation energies and forces exerted on small molecules by water using a GNN trained on a large dataset of mean explicit solvent forces containing 3 208 720 data points for chemically diverse organic molecules. The resulting ML model reaches the accuracy of explicit solvent reference simulations both in terms of reproducing reference forces of an external test set as well as conformational sampling in prospective MD simulations. The high transferability and an overall effective sampling speed-up of 18-fold compared to explicit solvent simulations allow the GNN to be used in practice as a general ML-based implicit solvent model for small organic molecules, the first of its kind. The approach is easy to use as it can be integrated into the commonly used OpenMM software package for MD simulation and only requires default OpenMM functions for parametrizing novel compounds. All data and source code are made freely available. In the future, we will employ the GNN in practical applications and expand the approach to other solvents as well as force-field representations (*e.g.*, polarizable force fields).

4 Methods

4.1 Molecular dynamics simulations

Starting coordinates for molecules were generated using the ETKDG conformer generator[31] as implemented in the RDKit.[32] The OpenFF 2.0.0 force field[33] was used to parametrize the compounds. All simulations were carried out using the OpenMM (version 8.0.0) simulation program.[34] For the explicit solvent simulations, the solutes were solvated with the TIP3P water model[35] in a box with a padding of 1 nm using the PACKMOL program.[36] Energy minimization was performed using the L-BFGS algorithm[37] with a tolerance of 10 kJ mol^{-1} nm^{-1}. The SETTLE[38] and CCMA[39] algorithms were used to constrain all bonds involving hydrogens for water and intra-molecular bonds, respectively. All simulations were carried out under Langevin dynamics using the LFMiddle discretization scheme,[40] a Monte Carlo barostat with a reference pressure of 1 bar, a reference temperature of 300 K, and a time step of 2 fs. Explicit solvent simulations were performed with a particle mesh Ewald (PME) correction[41] above a non-bonded cutoff of 1 nm.

4.2 Generation of the training and test sets

The molecules for the training set were taken from the DASH dataset.[21] The external test set was generated by drawing 1000 compounds at random from the QMUGS dataset[42] ensuring a molecular weight between 500 Da and 700 Da. The generation of the forces follows the general procedure described in ref. 12. For each molecule, three conformers were generated using the ETKDG conformer generator[31] as implemented in the RDKit.[32] These conformations were solvated and an explicit solvent simulation of 500 ps length was performed under NPT conditions. From this simulation, snapshots were extracted after 180 ps, 340 ps, and 500 ps. These snapshots served as starting

coordinates for new simulations of 200 ps length where the solute was positionally restrained. For each solute atom, the forces exerted by the solvent on the solute were averaged (write-out frequency of 200 fs). The mean forces were not further modified (*e.g.*, to make them translationally invariant). Note that not all compounds could be parametrized using the OpenFF force field and some simulations were unstable. Those compounds were excluded from the study as no mean forces could be extracted. The final data set is available at the ETH Research Collection (**https://www.research-collection.ethz.ch/handle/20.500.11850/667722**).

4.3 Graph neural networks

The core of the GNN was implemented as described in ref. 12 with the addition of the multitask SA term shown in eqn (1). During optimization, a random selection of 95% of all data points were used for training and the remaining 5% for validation. The GNN was trained for 30 epochs with a batch size of 32 and an exponentially decaying learning rate starting at 0.0005 and decaying to 0.000005. Gradients were clipped using a maximum norm of 1.0 and a norm type of 2. The Adam optimiser[43] was chosen for optimizing the network with the mean squared error (MSE) between the predicted forces and the explicit solvent reference forces F_{ref} as a loss function $\mathscr{L}$,

$$\mathscr{L} = \frac{1}{N} \sum_{n=1}^{N} \left| -\frac{\partial V^{GNN}}{\partial r}\bigg|_{r=r_n} - F_{ref,n} \right|^2 \tag{2}$$

4.4 Prospective molecular dynamics simulations

The OpenMM-Torch package (version 1.0, **https://github.com/openmm/openmm-torch**) was used to introduce the GNN on top of the vacuum Hamiltonian. The non-bonded forces were re-implemented using the OpenMM-Custom Forces classes for running multiple replicates of the system in parallel using one GNN. For the benchmarking of the GNN speed, compound **C3** was simulated with a replica size of 256 to optimize the simulation speed on the RTX 3090 GPU. The prospective simulations were carried out in 128 replicates to also allow the usage of GPUs with lower VRAM such as the RTX 1080TI or the RTX 2080TI. Note that while the replicates are of the same molecule in this study, they do not need to be and also 128 different molecules could be studied in one go. Explicit solvent TIP3P and GB-Neck2 simulations were performed for 500 ns. GNN simulations of each replicate for the molecules in set **I** and set **C** were carried out for 5 ns and 10 ns, respectively.

4.5 Data analysis

For analyzing the trajectories, MDTraj (version 1.9.7)[44] was used. The probability distributions for intramolecular hydrogen bond pairs or torsional angles were calculated by a histogram analysis. The free-energy profiles were than estimated using direct counting. For the atom–atom distances, a Jacobian correction factor of $4\pi r^2$ was applied.[45] The Wasserstein distances were calculated using the Python Optimal Transport

library[46] and the SciPy library[47] for two-dimensional and one-dimensional distributions, respectively.

Data and software availability

The code used to perform this study is open source and available on GitHub (https://github.com/rinikerlab/GNNImplicitSolvent). The training and test sets for the GNN are freely available at the ETH Research Collection (https://www.research-collection.ethz.ch/handle/20.500.11850/667722). Trajectories are available upon reasonable request from the corresponding author.

Author contributions

P. K.: conceptualization, data generation and curation, methodology, software, validation, visualization, writing – original draft. S. R.: conceptualization, funding acquisition, methodology, project administration, resources, supervision, writing – review and editing.

Conflicts of interest

There are no conflicts to declare.

Acknowledgements

References

1 T. Hansson, C. Oostenbrink and W. F. van Gunsteren, *Curr. Opin. Struct. Biol.*, 2002, **12**, 190–196.

2 J. Mortier, C. Rakers, M. Bermudez, M. S. Murgueitio, S. Riniker and G. Wolber, *Drug Discovery Today*, 2015, **20**, 686–702.

3 J. B. Metternich, P. Katzberger, A. S. Kamenik, P. Tiwari, R. Wu, S. Riniker and R. Zenobi, *J. Phys. Chem. A*, 2023, **127**, 5620–5628.

4 D. E. Shaw, P. Maragakis, K. Lindorff-Larsen, S. Piana, R. O. Dror, M. P. Eastwood, J. A. Bank, J. M. Jumper, J. K. Salmon, Y. Shan and W. Wriggers, *Science*, 2010, **330**, 341–346.

5 T.-S. Lee, D. S. Cerutti, D. Mermelstein, C. Lin, S. LeGrand, T. J. Giese, A. Roitberg, D. A. Case, R. C. Walker and D. M. York, *J. Chem. Inf. Model.*, 2018, **58**, 2043–2050.

6 A. S. Kamenik, S. M. Linker and S. Riniker, *Phys. Chem. Chem. Phys.*, 2022, **24**, 1225–1236.

7 B. Roux and T. Simonson, *Biophys. Chem.*, 1999, **78**, 1–20.

8 K. T. Butler, D. W. Davies, H. Cartwright, O. Isayev and A. Walsh, *Nature*, 2018, **559**, 547–555.

9 S. S. Mohamed Mahmoud, G. Esposito, G. Serra and F. Fogolari, *Bioinformatics*, 2020, **36**, 1757–1764.

10 D. Horvath, G. Marcou and A. Varnek, *J. Chem. Inf. Model.*, 2020, **60**, 2951–2965.

11 Y. Chen, A. Krämer, N. E. Charron, B. E. Husic, C. Clementi and F. Noé, *J. Chem. Phys.*, 2021, **155**, 084101.

12 P. Katzberger and S. Riniker, *J. Chem. Phys.*, 2023, **158**, 204101.

13 J. Airas, X. Ding and B. Zhang, *ACS Cent. Sci.*, 2023, **9**, 2286–2297.

14 H. Nguyen, D. R. Roe and C. Simmerling, *J. Chem. Theory Comput.*, 2013, **9**, 2020–2034.

15 N. A. Baker, *Curr. Opin. Struct. Biol.*, 2005, **15**, 137–143.

16 U. Haberthür and A. Caflisch, *J. Comput. Chem.*, 2007, **29**, 701–715.

17 C. W. Still, A. Tempczyk, R. C. Hawley and T. Hendrickson, *J. Am. Chem. Soc.*, 1990, **112**, 6127–6129.

18 M. Schaefer and M. Karplus, *J. Phys. Chem.*, 1996, **100**, 1578–1599.

19 E. J. M. Lang, E. G. Baker, D. N. Woolfson and A. J. Mulholland, *J. Chem. Theory Comput.*, 2022, **18**, 4070–4076.

20 R. Galvelis, A. Varela-Rial, S. Doerr, R. Fino, P. Eastman, T. E. Markland, J. D. Chodera and G. D. Fabritiis, *J. Chem. Inf. Model.*, 2023, **63**, 5701–5708.

21 M. T. Lehner, P. Katzberger, N. Maeder, C. C. G. Schiebroek, J. Teetz, G. A. Landrum and S. Riniker, *J. Chem. Inf. Model.*, 2023, **63**, 6014–6028.

22 M. L. Sanchez, M. A. Aguilar and F. J. O. del Valle, *J. Comput. Chem.*, 1997, **18**, 313–322.

23 D. M. Nikolaev, M. Manathunga, Y. Orozco-Gonzalez, A. A. Shtyrov, Y. O. G. Martínez, S. Gozem, M. N. Ryazantsev, K. Coutinho, S. Canuto and M. Olivucci, *J. Chem. Theory Comput.*, 2021, **17**, 5885–5895.

24 S. Yao, R. Van, X. Pan, J. H. Park, Y. Mao, J. Pu, Y. Mei and Y. Shao, *RSC Adv.*, 2023, **13**, 4565–4577.

25 B. Knapp, L. Ospina and C. M. Deane, *J. Chem. Theory Comput.*, 2018, **14**, 6127–6138.

26 X. Fu, Z. Wu, W. Wang, T. Xie, S. Keten, R. Gomez-Bombarelli and T. Jaakkola, Forces are not Enough: Benchmark and Critical Evaluation for Machine Learning Force Fields with Molecular Simulations, *arXiv*, 2022, preprint, arXiv:2210.07237, DOI: [10.48550/arXiv.2210.07237](https://doi.org/10.48550/arXiv.2210.07237).

27 D. L. Mobley and J. P. Guthrie, *J. Comput.-Aided Mol. Des.*, 2014, **28**, 711–720.

28 L. N. Vaserstein, *Probl. Peredachi Inf.*, 1969, **5**, 64–72.

29 M. Thürlemann and S. Riniker, *J. Chem. Phys.*, 2023, **159**, 024105.

30 R. Anandakrishnan, A. Drozdetski, R. C. Walker and A. V. Onufriev, *Biophys. J.*, 2015, **108**, 1153–1164.

31 S. Riniker and G. A. Landrum, *J. Chem. Inf. Model.*, 2015, **55**, 2562–2574.

32 Open-source cheminformatics toolkit, 2022.09.1 (Q3 2022) Release, 2022, http://www.rdkit.org, accessed: April 12, 2024.

33 S. Boothroyd, P. K. Behara, O. C. Madin, D. F. Hahn, H. Jang, V. Gapsys, J. R. Wagner, J. T. Horton, D. L. Dotson, M. W. Thompson, J. Maat, T. Gokey, L.-P. Wang, D. J. Cole, M. K. Gilson, J. D. Chodera, C. I. Bayly, M. R. Shirts and D. L. Mobley, *J. Chem. Theory Comput.*, 2023, **19**, 3251–3275.

34 P. Eastman, J. Swails, J. D. Chodera, R. T. McGibbon, Y. Zhao, K. A. Beauchamp, L.-P. Wang, A. C. Simmonett, M. P. Harrigan, C. D. Stern, R. P. Wiewiora, B. R. Brooks and V. S. Pande, *PLoS Comput. Biol.*, 2017, **13**, e1005659.

35 W. L. Jorgensen, J. Chandrasekhar, J. D. Madura, R. W. Impey and M. L. Klein, *J. Chem. Phys.*, 1983, **79**, 926–935.

36 L. Martínez, R. Andrade, E. G. Birgin and J. M. Martínez, *J. Comput. Chem.*, 2009, **30**, 2157–2164.

37 D. C. Liu and J. Nocedal, *Math. Program.*, 1989, **45**, 503–528.

38 S. Miyamoto and P. A. Kollman, *J. Comput. Chem.*, 1992, **13**, 952–962.

39 P. Eastman and V. S. Pande, *J. Chem. Theory Comput.*, 2010, **6**, 434–437.

40 Z. Zhang, X. Liu, K. Yan, M. E. Tuckerman and J. Liu, *J. Phys. Chem. A*, 2019, **123**, 6056–6079.

41 T. Darden, D. York and L. Pedersen, *J. Chem. Phys.*, 1993, **98**, 10089–10092.

42 C. Isert, K. Atz, J. Jiménez-Luna and G. Schneider, *Sci. Data*, 2022, **9**, 273.

43 D. P. Kingma and J. Ba, Adam: A Method for Stochastic Optimization, *arXiv*, 2014, preprint, arXiv:1412.6980, DOI: **10.48550/arXiv.1412.6980**.

44 R. T. McGibbon, K. A. Beauchamp, M. P. Harrigan, C. Klein, J. M. Swails, C. X. Hernández, C. R. Schwantes, L.-P. Wang, T. J. Lane and V. S. Pande, *Biophys. J.*, 2015, **109**, 1528–1532.

45 D. R. Herschbach, H. S. Johnston and D. Rapp, *J. Chem. Phys.*, 1959, **31**, 1652–1661.

46 R. Flamary, N. Courty, A. Gramfort, M. Z. Alaya, A. Boisbunon, S. Chambon, L. Chapel, A. Corenflos, K. Fatras, N. Fournier, L. Gautheron, N. T. Gayraud, H. Janati, A. Rakotomamonjy, I. Redko, A. Rolet, A. Schutz, V. Seguy, D. J. Sutherland, R. Tavenard, A. Tong and T. Vayer, *J. Mach. Learn. Res.*, 2021, **22**, 1–8.

47 P. Virtanen, R. Gommers, T. E. Oliphant, M. Haberland, T. Reddy, D. Cournapeau, E. Burovski, P. Peterson, W. Weckesser, J. Bright, S. J. van der Walt, M. Brett, J. Wilson, K. J. Millman, N. Mayorov, A. R. J. Nelson, E. Jones, R. Kern, E. Larson, C. J. Carey, İ. Polat, Y. Feng, E. W. Moore, J. VanderPlas, D. Laxalde, J. Perktold, R. Cimrman, I. Henriksen, E. A. Quintero, C. R. Harris, A. M. Archibald, A. H. Ribeiro, F. Pedregosa and P. van Mulbregt, SciPy 1.0 Contributors, *Nat. Methods*, 2020, **17**, 261–272.